

LA-UR- 01 - 4476

Approved for public release;  
distribution is unlimited.

Title: Small-Signal Analysis and Particle-In-Cell Simulations of  
Planar Dielectric Cherenkov Masers for Use as  
High-Frequency, Moderate-Power Broad-Band Amplifiers

Author(s): Bruce E. Carlsten

Submitted to: Physics of Plasmas



## Los Alamos

NATIONAL LABORATORY

Los Alamos National Laboratory, an affirmative action/equal opportunity employer, is operated by the University of California for the U.S. Department of Energy under contract W-7405-ENG-36. By acceptance of this article, the publisher recognizes that the U.S. Government retains a nonexclusive, royalty-free license to publish or reproduce the published form of this contribution, or to allow others to do so, for U.S. Government purposes. Los Alamos National Laboratory requests that the publisher identify this article as work performed under the auspices of the U.S. Department of Energy. Los Alamos National Laboratory strongly supports academic freedom and a researcher's right to publish; as an institution, however, the Laboratory does not endorse the viewpoint of a publication or guarantee its technical correctness.

# Small-Signal Analysis and Particle-in-Cell Simulations of Planar Dielectric Cherenkov Masers for Use as High-Frequency, Moderate-Power Broad-Band Amplifiers

Bruce Carlsten

Los Alamos National Laboratory

Los Alamos, NM 87544

*Abstract:* A small-signal gain analysis of the planar dielectric Cherenkov maser is presented. The analysis results in a Pierce gain solution, with three traveling-wave modes. The analysis shows that the dielectric cherenkov maser has remarkable broad-band tuning ability near cutoff, while maintaining reasonable gain rates. Numerical simulations verifying the small-signal gain results are presented, using a new particle-in-cell code written specifically for planar traveling-wave tubes. Instantaneous bandwidth is numerically shown to also be very large, and saturated efficiency for a nominal high-power design is shown to be in the range of standard untapered traveling-wave tubes.

## I. Analysis

Traveling-wave interactions between electron beams and waveguide modes in dielectrically loaded waveguides have been studied in detail for some time. These types of devices are commonly known as dielectric Cherenkov masers (DCMs). The basic principle of operation is based on slowing down the phase velocity of the waveguide mode by lining the waveguide with a dielectric until it is synchronous with the electron beam velocity, and then the waveguide mode and electron beam interact in a manner essentially the same as in the common traveling-wave tube (TWT) [1,2]. As with all TWT interactions, the DCM interaction is capable of high power, high gain, and large bandwidth. The traveling-wave interaction between an electron beam and an rf mode with a uniform phase velocity is not particularly high, typically 20-30% [3], but this base

efficiency can be greatly increased by tapering the phase velocity of the waveguide mode and using a multi-stage depressed collector. An X-band DCM with a tapered dielectric had simulated efficiencies of 37%, and experimentally yielded an output power of 280 MW [4]. Tapering the dielectric will tend to reduce bandwidth, and a careful tradeoff must be made tailored for the specific application.

Most previous work on DCMs has been focused on producing high power, varying in frequency up to 100 GHz. In addition, all previous work has focused on DCMs with cylindrical geometries. New emerging low-power communication needs has motivated a study of low-power DCMs with low fabrication cost. An attractive potential configuration is to use a planar DCM with a low-power electron beam generated by field emitter arrays (FEAs) [5]. An electron source using the emerging FEA technology instead of a conventional thermionic electron gun technology has smaller size and less weight, both key advantages for low-power communication tubes. Issues with using FEAs have been addressed in previous experimental programs, and a pencil-beam 4.5 GHz TWT with 17% extraction efficiency and 35 dB of gain has been demonstrated at Northrup Grumman [6]. Cathode loadings in excess of  $10 \text{ A/cm}^2$  have been demonstrated [5,6]. FEAs have already demonstrated total beam currents on the order of 1 A for cylindrical beams.

Use of the DCM interaction provides great tunability range (by varying the beam voltage), with reasonable gain and the potential for satisfactory efficiency (with tapering and a depressed collector). The planar geometry provides scalability to large-scale microfabrication techniques, resulting in low fabrication cost. An alternative planar source geometry also suitable for large-scale microfabrication is to use a sheet electron beam in a rippled waveguide. This type of TWT tends to have higher gain and can operate at a higher frequency for the same beam voltage [7], but does not have the wide tunability range of the DCM. For many low-power communication applications, the planar DCM would be a better choice.

For scaling studies, a simple analytic formula for the gain is desirable. The primary goal of this paper is to provide such a simple gain formula, for a planar DCM. To verify the small-signal results, a particle-in-cell (PIC) code, TUBE, was developed for simulating the planar DCM interaction. This code uses an unusual charge-conserving current algorithm [8] to eliminate the Poisson solve step in the field advance. This code is described in detail in this paper. In the final section of this paper, a high-power simulation case is presented, demonstrating the large range of accuracy of the small-signal gain formula derived earlier.

## II. Small-signal gain analysis

We consider the geometry shown in Fig. 1, where a planar electron beam of width  $\Delta$  travels down a waveguide of infinite transverse width with total half-width  $r_w$ . A dielectric liner is placed between the vertical positions  $r_d$  and  $r_w$ . The region below  $r_d$  is referred to as I and the region between  $r_d$  and  $r_w$  is referred to as II. The dielectric material has total dielectric constant  $\epsilon_r \epsilon_0$ , where  $\epsilon_0$  is the permittivity of free space.

We limit this analysis to TM modes, where there is only a horizontal component to the magnetic field. We also assume an exponential dependence of  $e^{j(\omega t - kz)}$ , and where  $\omega/k$  needs to be close to the beam velocity  $v_0$  for proper synchronism. Use of the wave equation immediately gives

$$B_{x,I} = a_I \cos(h_I y) + b_I \sin(h_I y) \quad (1)$$

and

$$B_{x,II} = a_{II} \cos(h_{II} y) + b_{II} \sin(h_{II} y) \quad , \quad (2)$$

where

$$h_I^2 = \frac{\omega^2}{c^2} - k^2 \quad (3)$$

which is less than zero and

$$h_{II}^2 = \frac{\omega^2}{c^2} \varepsilon_r - k^2 \quad , \quad (4)$$

which needs to be greater than zero.

Two useful relations relating the electric field to the horizontal magnetic field is given by

$$E_z = \frac{j}{\omega \varepsilon \mu_0} \frac{\partial B_x}{\partial y} \quad (5)$$

and

$$E_y = -\frac{j}{\omega \varepsilon \mu_0} \frac{\partial B_x}{\partial z} \quad . \quad (6)$$

We find the dispersion relation for this interaction by using Gauss' law at the beam, and the conduction boundary condition at  $r_w$  (axial electric field vanishes), and matching the region solutions at  $r_d$  (the axial electric field is continuous and the radial electric field times  $\varepsilon$  is continuous).

Gauss' law at  $y = 0$  yields

$$E_{y,I} = \frac{\rho \Delta}{2\varepsilon_0} \quad . \quad (7)$$

The rf charge density  $\rho$  is related to the axial electric field by

$$\rho = \frac{jk\rho_0 e E_{z,I}}{m\gamma^3(\omega - kv_0)^2} , \quad (8)$$

where  $\rho_0$  is the DC charge density,  $e$  is the electronic charge,  $m$  is the electronic mass, and  $\gamma$  is the relativistic mass factor.

Equations (1)-(4) give this relation between the constants for region I:

$$a_I = b_I \frac{\Delta\rho_0 e h_I}{2\varepsilon_0 m \gamma^3 (\omega - kv_0)^2} . \quad (9)$$

Using  $I_A = 4\pi\varepsilon_0 mc^3 / e$  and recognizing that the total beam current is  $I = -v_0 \rho_0 \Delta W$  where  $W$  is the beam width, this becomes

$$a_I = -b_I \frac{I}{I_A} \frac{2\pi h_I c^3}{W v_0 \gamma^3 (\omega - kv_0)^2} . \quad (10)$$

For convenience, we will define

$$C_I = -\frac{I}{I_A} \frac{2\pi h_I c^3}{W v_0 \gamma^3 (\omega - kv_0)^2} . \quad (11)$$

The boundary condition at  $r_w$  gives us

$$a_{II} = b_{II} \frac{\cos(h_{II} r_w)}{\sin(h_{II} r_w)} , \quad (12)$$

and we will additionally define

$$C_{II} = \frac{\cos(h_{II}r_w)}{\sin(h_{II}r_w)} . \quad (13)$$

The axial boundary condition at  $r_d$  is

$$(-a_{II} \sin(h_{II}r_d) + b_I \cos(h_{II}r_d))h_{II} = (-a_{II} \sin(h_Ir_d) + b_I \cos(h_Ir_d))h_I \quad (14)$$

and the radial boundary condition is

$$(a_{II} \cos(h_{II}r_d) + b_I \sin(h_{II}r_d))\varepsilon_r = (a_{II} \cos(h_Ir_d) + b_I \sin(h_Ir_d)) \quad (15)$$

These equations immediately reduce to the dispersion relation

$$h_{II} \frac{\left( \cos(h_{II}r_d) - \frac{\cos(h_{II}r_w)}{\sin(h_{II}r_w)} \sin(h_{II}r_d) \right)}{\left( \sin(h_{II}r_d) + \frac{\cos(h_{II}r_w)}{\sin(h_{II}r_w)} \cos(h_{II}r_d) \right)} = h_I \frac{(\cos(h_Ir_d) - C_I \sin(h_Ir_d))}{(\sin(h_Ir_d) + C_I \cos(h_Ir_d))} \varepsilon_r , \quad (16)$$

or

$$h_{II} \tan(h_{II}(r_w - r_d)) = h_I \cot(h_I(r_d - \varphi))\varepsilon_r , \quad (17)$$

where  $\varphi$  is a small angle, given by

$$\tan(h_I\varphi) = C_I , \quad (18)$$

which is small for moderate currents.

At this point, we will find the cold synchronism equation by assuming that  $C_I$  vanishes and that  $r_d$  is very small (relative to a free-space wavelength). The idea is to first find a rough relation between  $\omega$  and  $k$ , and then to expand about this cold solution in the presence of a small-current beam as a perturbation.

For small  $r_d$  and no current, the dispersion relation reduces to

$$\frac{1}{\varepsilon_r} h_{II} \tan(h_{II}(r_w - r_d)) = \frac{1}{r_d} . \quad (19)$$

We know that  $h_{II}(r_w - r_d)$  must be close to  $\pi/2$ , so the left-hand side of Eqn. (19) reduces to

$$\frac{1}{\varepsilon_r} h_{II} \frac{1}{\pi/2 - h_{II}D} = \frac{1}{r_d} , \quad (20)$$

where we are using  $D = (r_w - r_d)$  for the depth of the dielectric liner. We can solve the above equation for  $h_{II}$ , yielding

$$h_{II} = \frac{\pi/2}{D + r_d / \varepsilon_r} . \quad (21)$$

Using Eqn. (4) and invoking single-particle synchronism ( $k = \omega/v_0$ ), we get this relation:

$$k^2 = \frac{\omega^2}{v_0^2} = \frac{\omega^2 \varepsilon_r}{c^2} - \left( \frac{\pi/2}{D + r_d / \varepsilon_r} \right)^2 \quad (22)$$

or



$$\omega = \frac{\pi/2}{(D + r_d/\epsilon_r) \sqrt{\frac{\epsilon_r}{c^2} - \frac{1}{v_0^2}}} . \quad (23)$$

This equation establishes the synchronous frequency of the dielectric-loaded TWT, given beam velocity, relative permittivity, and dimensions of both the waveguide and dielectric.

Now we want to find the gain for nonzero current. We do this by going back to Eqn. (17), but now with  $C_I$  small, but nonzero. The new reduced dispersion relation is now

$$\frac{1}{\epsilon_r} h_{II} \frac{1}{\pi/2 - h_{II} D} = \frac{1}{r_d + \frac{K}{(\omega - v_0 k)^2}} , \quad (24)$$

where we have collected several constants into  $K$ .

We assume we can write the wavenumber as

$$k = k_0 + \delta k , \quad (25)$$

where

$$k_0 = \omega / v_0 , \quad (26)$$

and is the cold synchronism wavenumber.

Using  $\delta h_{II} = -\frac{k}{h_{II}} \delta k$  and expanding to first order, we have

$$h_{II} \frac{r_d}{\epsilon_r} + \delta h_{II} \frac{r_d}{\epsilon_r} + h_{II} \frac{K}{\epsilon_r v_0^2 (\delta k)^2} = \frac{\pi}{2} - h_{II} D - \delta h_{II} D \quad , \quad (27)$$

or

$$\frac{h_{II} K}{\epsilon_r v_0^2 (\delta k)^2} = \delta k \frac{k}{h_{II}} \left( D + \frac{r_d}{\epsilon_r} \right) \quad . \quad (28)$$

Putting the constants back in, we have

$$(\delta k)^3 = - \frac{h_{II}^2}{(\epsilon_r D + r_d) k} \frac{(I / I_A) 2\pi c^3}{W v_0^3 \gamma^3} = - \frac{(\pi / 2)^2}{(\epsilon_r D + r_d)^3 (\omega / v_0)} \frac{(I / I_A) 2\pi c^3}{W v_0^3 \gamma^3} = -C^3 \quad , \quad (29)$$

where we have defined the Pierce constant  $C$  in terms of the constants. The total wavenumber for the growing mode is then

$$k = \omega / v_0 + \left( \frac{\sqrt{3}}{2} + \frac{j}{2} \right) C \quad , \quad (30)$$

and the exponential gain goes as

$$e^{Cz/2} \quad . \quad (31)$$

Note that the above perturbation analysis is valid as long as  $C \ll \omega / v_0$ , and is only strictly valid at the single-particle synchronism; for low-power applications at the frequencies that we are interested in ( $\sim 100$  GHz), these are not an important limitations.

The loss introduced by an imaginary component of the dielectric constant can be found from Eqn. (22). Taking derivatives, we find

$$2k\delta k_{loss} = j\delta\epsilon_{imag} \left( -\frac{\omega^2}{c^2} - \frac{r_d\pi/2}{\epsilon_r^2(D+r_d/\epsilon_r)^2} \right) . \quad (32)$$

For large dielectric constants, we can ignore the second term, and the modified wavenumber becomes

$$k = \omega / v_0 + \left( \frac{\sqrt{3}}{2} + \frac{j}{2} \right) C - j \frac{v_0\omega}{2c^2} \delta\epsilon_{imag} . \quad (33)$$

The wide resonance dependence on beam voltage is shown in Fig. 2, for various relative permittivities, using Eqn. (23). Relatively small voltage changes near  $\epsilon_r \sim \sqrt{c/v_0}$  can lead to very large frequency changes, leading to an extremely large tunable bandwidth with little changes in the beam voltage. The practical limitation on how close to the knee a DCM can operate will be established by voltage tolerances and physical energy spread on the electron beam.

In Fig. 3, we plot gain versus dielectric constant for a 1 A beam at 75 kV. Relatively high gains (1 dB/cm) are achievable. In Fig. 4, we plot gain versus beam voltage, for a 1 A beam and a dielectric with a relative permittivity of 30.

### **III. Description of Traveling-Wave-Tube Simulation Code**

A new variant of the ISIS particle-in-cell (PIC) code [9] was generated for simulating the planar DCM device. This new code, TUBE, was written in order to tailor the simulation specifically for the traveling-wave interaction, increasing computation speed. Specifically, less dense particle injection is needed for modeling traveling-wave tubes than for general plasma problems. The electromagnetic fields are solved on a grid using Maxwell's curl equations, as done by Shintake [10] for klystron simulations. The general procedure of evolving the electromagnetic fields is well known [11], but will be described below for clarity.

A typical issue in PIC codes is ensuring conservation of charge. Analytically, this is guaranteed by the magnetic field curl equation and the continuity equation; however, when these equations are discretized on a mesh in a PIC simulation, numerical errors lead to a (typically) linear increase in the error in the fields. This is because the discretized current density that actually conserves charge is not a linear weighing of the movement of charge on the mesh. In fact, it cannot be generated by just using the instantaneous movement of charge on the mesh. This effect is well known [11-13] and the usual technique to correct this is requires a separate Poisson solve step each time the electromagnetic fields are evolved.

In 1968 Buneman suggested a charge-conserving current algorithm [14], where the current density used in the magnetic field curl equation is derived by explicitly finding what is required to conserve charge, where each particle in the simulation is a point particle. Morse and Nielson [12] wrote an improved two-dimensional version of this idea, using particles with rectangular shape. Both of these techniques lead to noise in the simulations because there is a sudden impulse in the current density when a particle crosses from one cell in the mesh to another [13]. The level of noise in these simulations still required a Poisson solve to maintain stability. Jones [8] reduced the noise dramatically by using triangular shaped particles (pyramidal in two-dimensional

geometries), which does not require a Poisson solve, and is the charge-conserving current algorithm used in the ISIS code. Because this algorithm executes very efficiently, it was adapted for TUBE.

A PIC code is required for accurate traveling-wave tube simulations because of the importance of space-charge forces in many possible DCM configurations. The importance of space charge is easily shown by considering the potential depression of a planar beam in a planar waveguide.

The potential depression for an infinitely thin sheet beam in a waveguide of half-height  $r_w$  is given by

$$\phi(r) = \frac{I_o}{2v_o W} \left( \frac{r_d}{\epsilon_0} + \frac{r_w - r_d}{\epsilon_0 \epsilon_r} \right) \quad (34)$$

where

$$v_o = c \sqrt{1 - \left( \gamma_{inj} - \frac{e\phi_b}{mc^2} \right)^{-2}}, \quad (35)$$

$\phi_b$  is the beam potential, and  $\gamma_{inj}$  is the relativistic mass factor corresponding to the injection voltage. Rewriting this, we have

$$\frac{e\phi_b}{mc^2} \sqrt{1 - \left( \gamma_{inj} - \frac{e\phi_b}{mc^2} \right)^{-2}} = \left( r_d + \frac{r_w - r_d}{\epsilon_r} \right) \frac{2\pi I_o}{I_A W}. \quad (36)$$

Following references 15 and 16, we can differentiate this with respect to  $\phi_b$  to get maximum allowable current, the space-charge limited current. We find that  $I_o$  is maximized when

$$e\phi_b = (\gamma_{inj} - \gamma_{inj}^{1/3})mc^2 \quad (37)$$

and is given by

$$I_{scl} = \frac{I_A W}{2\pi(r_d - (r_w - r_d)/\epsilon_r)} (\gamma_{inj}^{2/3} - 1)^{3/2} . \quad (38)$$

Rewriting this in terms of minimum transmittable beam energy for a given peak current we get:

$$\gamma_{min}^{2/3} = \left( \frac{I_{peak}}{I_A W} \left( r_d - \frac{r_w - r_d}{\epsilon_r} \right) 2\pi \right)^{2/3} + 1 . \quad (39)$$

This expression is important because the maximum power we can extract is given by

$$P_{max} = \frac{1}{2} I_1 (511 \text{ kV}) (\gamma_{inj} - \gamma_{min}) \quad (40)$$

where  $I_1$  is the beam's harmonic current. If we consider a 15 A sheet beam that is 1 cm wide in a 2-mm high waveguide (with no dielectric liner), the minimum allowable mass factor  $\gamma_{min}$  is 1.0101, or the minimum allowable beam energy (kinetic plus potential depression) is 5.2 kV. Thus, for a beam injected at 10 kV, only 4.8 kV of kinetic energy can be extracted (less if there is significant beam bunching), before a virtual cathode is formed. To minimize this effect, a small waveguide height and a high beam voltage are desired.

In order to ensure that the space-charge fields are found with sufficient accuracy, the electromagnetic fields are solved on the grid shown in Fig. 5. The fields are evolved in time by explicitly solving discrete versions of the curl equations  $\frac{\partial \vec{B}}{\partial t} = -\vec{\nabla} \times \vec{E}$  and

$\frac{\partial \vec{E}}{\partial t} = c^2 (\vec{\nabla} \times \vec{B} - \mu_o \vec{J})$  for each cell on the PIC grid. The grid locations for TM mode components are shown in Fig. 6, for grid cell (i,j).

The electric and magnetic fields are separately evolved simultaneously (leapfrogging leads to an instability). After time stepping the fields, boundary conditions are established by setting by making  $E_r$  or  $E_z$  vanish on the conduction boundary. The upstream and downstream ends of the beam pipe are made to be conducting surfaces (shown in Fig. 5). This guarantees evolving the correct potential depression for the beam as it is injected through the upstream boundary. The simulation starts with  $\vec{E} = \vec{B} = 0$  everywhere, and the beam current follows an exponential increase from zero over several rf periods to steady state. The fields from an initial rf cavity is superimposed onto the space-charge fields to supply the input for the traveling-wave interaction.

It is simple to show that the divergence equations  $\vec{\nabla} \cdot \vec{E}$  and  $\vec{\nabla} \cdot \vec{B}$  are satisfied by the curl equations and the initial conditions on the fields [11]. The  $\vec{\nabla} \cdot \vec{B}$  equation is satisfied trivially:

$$\frac{\partial}{\partial t} (\vec{\nabla} \cdot \vec{B}) = \vec{\nabla} \cdot \frac{\partial \vec{B}}{\partial t} = -\vec{\nabla} \cdot \vec{\nabla} \times \vec{E} = 0 \quad . \quad (41)$$

The conservation of charge equation,  $\vec{\nabla} \cdot \vec{E}$ , requires use of continuity equation [11],

$$\vec{\nabla} \cdot \vec{J} = -\frac{\partial \rho}{\partial t} \quad , \quad (42)$$

$$\begin{aligned} \frac{\partial}{\partial t} \left( \vec{\nabla} \cdot \vec{E} - \frac{\rho}{\epsilon_o} \right) &= \vec{\nabla} \cdot \frac{\partial \vec{E}}{\partial t} - \frac{1}{\epsilon_o} \frac{\partial \rho}{\partial t} \\ &= c^2 \vec{\nabla} \cdot \vec{\nabla} \times \vec{B} - c^2 \mu_o \vec{\nabla} \cdot \vec{J} - \frac{1}{\epsilon_o} \frac{\partial \rho}{\partial t} = -\frac{1}{\epsilon_o} \left( \vec{\nabla} \cdot \vec{J} + \frac{\partial \rho}{\partial t} \right) \quad . \end{aligned} \quad (43)$$

Thus numerical conservation of charge is equivalent to ensuring that the numerical form of the continuity equation is satisfied. Unfortunately, simple assignment of charge and current density onto the grid starting with the physical particle positions and their instantaneous movement with any weighing scheme will not satisfy it. The current density assigned to the grid must in fact be derived from requiring that the discrete continuity equation be satisfied.

Morse's and Nielson's charge-conserving current algorithm can be easily described for the one-dimensional case, pictured in Fig. 7, following the discussion in reference 8. The charge density is assigned to the grid intersection points and the current density is assigned to locations at the centers of the grid cells. The charge density is assigned at the standard time-step intervals and the current density is assigned at half time-step intervals. The charge weighing on the grid is assumed to be linear. A particle with charge  $q$  in cell  $i$  distributes a charge  $\left(1 - \frac{\Delta x}{dx}\right)q$  at grid intersection point  $i$  and  $\frac{\Delta x}{dx}q$  at grid intersection point  $i+1$ , where  $dx$  is the grid spacing and  $\Delta x$  is the distance the particle is from grid intersection point  $i$ . If the particle does not change cells during a time step of duration  $dt$ , current is only assigned to location  $i$ , and is given by  $q\delta/dt$  for a movement  $\delta$ . This assignment explicitly satisfies the discrete version of the continuity equation

$$\frac{\rho(i, t+dt) - \rho(i, t)}{dt} = - \frac{J(i, t+dt/2) - J(i-1, t+dt/2)}{dx}, \quad (44)$$

where  $\rho$  is the charge density assigned to grid intersection point  $i$  at time  $t$ , and  $J$  is the current density assigned to mid-grid point  $i$  at time  $t+dt/2$ . For this case,  $J(i-1, t+dt/2)$  is zero and the continuity equation is satisfied.

Now consider the case where the particle moves from cell  $i$  to cell  $i+1$  during the time interval  $t$  to  $t+dt$ , from location  $\Delta x_i$  in cell  $i$  to location  $\Delta x_{i+1}$  in cell  $i+1$ . The discrete continuity equation is satisfied with these assignments:



$$\rho(i, t) = \left(1 - \frac{\Delta x_i}{dx}\right) q \quad (45)$$

$$\rho(i, t + dt) = 0 \quad (46)$$

$$\rho(i + 1, t) = \frac{\Delta x_i}{dx} q \quad (47)$$

$$\rho(i + 1, t + dt) = \left(1 - \frac{\Delta x_{i+1}}{dx}\right) q \quad (48)$$

$$\rho(i + 2, t) = 0 \quad (49)$$

$$\rho(i + 2, t + dt) = \frac{\Delta x_{i+1}}{dx} q \quad (50)$$

$$J(i, t + dt/2) = \left(1 - \frac{\Delta x_i}{dx}\right) q \frac{dx + \Delta x_{i+1} - \Delta x_i}{dt} \quad (51)$$

and

$$J(i + 1, t + dt/2) = \frac{\Delta x_{i+1}}{dx} q \frac{dx + \Delta x_{i+1} - \Delta x_i}{dt} \quad (52)$$

Some noise is generated by the linear weighting of the particles. This noise is greatly reduced by using a triangular particle shape and quadratic weighing [8].

When a particle moves diagonally into cells that touch at corners in a two-dimensional grid, there is an ambiguity – did the particle first move vertically into a new cell and then horizontally into the final cell, or did the particle first move horizontally and then vertically. Each path leads to different discrete current densities from the continuity

equation. For the algorithm used in ISIS and TUBE, it is assumed that half of a particle's charge takes one path and that half takes the other path [8].

The PIC simulation needs smoothing and damping to eliminate noise and numerical instabilities. This noise arises from many areas, and the two major effects are:

1. Noise from reflections off the metallic boundaries of high-harmonic field modes.
2. Grid instability from the roll-off of the dispersion relation for waveguide modes with wavelengths on the order of the mesh size.

To address these problems, TUBE uses two smoothing and damping algorithms. The first is to numerically include lossy material at both upstream and downstream boundaries, using the equations

$$\frac{\partial \vec{E}}{\partial t} = c^2 (\vec{\nabla} \times \vec{B} - \mu_o \vec{J}) - \sigma_1 \vec{E} \quad (53)$$

or

$$\frac{\partial \vec{B}}{\partial t} = -\vec{\nabla} \times \vec{E} - \sigma_2 \vec{B} \quad (54)$$

The second technique is two stage smoothing, as used in Shintake's code FCI [10]. Smoothing is done in two successive steps, using the equations

$$\begin{aligned} \rho(i, j) &= \frac{\rho(i-1, j) + 2\rho(i, j) + \rho(i+1, j)}{4} \\ \rho(i, j) &= \frac{-\rho(i-1, j) + 6\rho(i, j) - \rho(i+1, j)}{4} \end{aligned} \quad (55)$$

The second step is a compensation step to regain higher harmonic content. The resulting transfer function from this smoothing is given by  $G = 1 - \frac{1}{16}(k\Delta z)^4$ , which translates to less than 1% amplitude loss at the 3<sup>rd</sup> harmonic, for typical grid spacings [10].

We can verify the numerical stability of the simulation model (including the charge-conserving current algorithm) by considering the case with no rf input drive. In Fig. 8a we plot the vertical electric field at a position above the beam. The field is stable, in the sense of both nongrowing and nonoscillating. This simulation is for a sheet beam of 15 A per cm width in a 2 mm high waveguide, for a total length of 12 cm. The vertical electric field is measured 0.5 mm from the top wall, at a length of 6 cm. The beam voltage is 25 kV. This case corresponds to simulations in the next section, except that the beam voltage is lower; this was done to increase the relative potential depression of the simulation. In Fig. 8b, we see that the potential depression of the beam is symmetric between the conducting endplates of the simulation region and well behaved.

#### IV. Numerical Simulations Showing Gain and Saturation

In this section, we consider the case of a 15-A, 1-cm wide beam in a 2-mm high waveguide, injected at 140 kV. The generation and transport of this 2.1 MW beam has been considered for a W-band klystron, and is credible using current technology [17]. We will assume that a dielectric of width 0.54 mm is lining the waveguide, with dielectric constant 30. In this section, we present a relatively high power case, to show the range of the small-signal gain formula and to show a more interesting PIC simulation.

The analytic theory of the second section yields a single-particle resonance at 25.7 GHz, with a gain of 0.38 dB/m. Gain results from a frequency scan using TUBE are shown in Fig. 9. Although the analytic gain prediction is nearly exact (at 25.7 GHz), the peak of the gain curve is higher (over twice as high) at a somewhat higher frequency. Recall that the analytic formula assumed the single particle resonance  $k = \omega / v_0$ , to establish a value for  $k$ , between the left-hand side and the right-hand side of Eqn. (29). The left-hand side

is very accurate for all  $k$ , however,  $k$  in general requires solving a transcendental equation. For low power cases,  $k$  is very close to the single-particle resonance for all modes with gain. However, as the beam current is increased,  $k$  can change from that, as the resonance is between the rf mode's phase velocity and the slow-space-charge wave of the beam. This effect is seen in this simulation, and the maximum gain occurs off the single-particle resonance.

In Fig. 10, we show the particles' modulation exponential increase as a function of axial location, for the peak gain of 1.2 dB/cm, at 28.7 GHz. For the case shown in Fig. 11, the input drive was increased, and saturation was reached over a length of 12 cm. The extraction efficiency for this case (also at 28.7 GHz) is nearly 20%.

These simulations verify the key aspects of planar DCM design and operation. First, the analytic theory accurately predicts the gain at the frequency corresponding to single-particle synchronism. Next, maximum gain occurs at a frequency that deviates from the single-particle synchronism, but is of the same order of magnitude, even for very high-power cases. Finally, the extraction efficiency of this device is similar to others with traveling-wave interactions, on the order of 15-25% for an untapered device.

In addition, we have demonstrated the operation and stability of a PIC code tailored for sheet-beam TWT interactions, using a noiseless charge-conserving current algorithm and two-stage smoothing.

## Acknowledgments

The author wishes to acknowledge Michael Jones' clear and lucid teachings and his tremendous patience in introducing and tutoring the author in writing and using PIC codes for accelerator and microwave tube simulations. Dr. Jones' many contributions to plasma physics and numerical simulations will be remembered, and he will be sorely missed by his friends and colleagues.

This work was supported by the Los Alamos National Laboratory Directed Research and Development program.

## References

1. J. E. Walsh, and J. B. Murphy, *IEEE J. Quant. Elec.*, **18**, 1259 (1982).
2. E. P. Garate and J. E. Walsh, "The Cherenkov maser at millimeter wavelengths," *IEEE Trans. Plasma Sci.*, **13**, 524 (1985).
3. D. J. Angelakos and T. E. Everhart, Microwave Communication, McGraw-Hill Book Company, New York (1968).
4. W. Peter, E. Garate, W. Main, and A. Fisher, "High-gain X-band dielectric cherenkov maser," *Phys. Rev. Lett.*, **65**, 2989 (1990).
5. K. L. Jensen, "Field emitter arrays for plasma and microwave source applications," *Phys. Plasmas*, **6**, 2241 (1999).
6. D. R. Whaley, B. M. Gannon, C. R. Smith, C. M. Armstrong, and C. A. Spindt, "Application of field emitter arrays to microwave power amplifiers," *IEEE Trans. Plasma Sci.*, **28**, 727 (2000).
7. B. E. Carlsten, "Pierce gain analysis for a sheet electron beam in a rippled waveguide traveling-wave tube," *Phys. Plas.* **XX**, yy (2001).
8. M. E. Jones, private communication, 1985.
9. G. Gisler, M. E. Jones, and C. M. Snell, *Bull Am. Phys. Soc.*, **29**, 1208 (1984).
10. T. Shintake, "Klystron simulation and design using the field charge interaction (FCI) code," *Nucl. Instrum. Methods Phys. Res. A*, **363**, 83 (1995).
11. C. K. Birdsall and A. B. Langdon, Plasma Physics via Computer Simulation, McGraw-Hill Book Company, New York (1985).
12. R. L. Morse and C. W. Nielson, "Numerical simulation of the Weibel instability in one and two dimensions," *Phys. Fluids*, **14**, 830 (1971).
13. A. B. Langdon, "Some electromagnetic plasma simulation methods and their noise properties," *Phys. Fluids*, **15**, 1149 (1972).
14. O. Buneman in Relativistic Plasmas, edited by O. Buneman and W. Pardo, Benjamin, New York, 205 (1968).

15. R. B. Miller, An Introduction of the Physics of Intense Charged Particle Beams, New, York, Plenum, 1982.
16. B. E. Carlsten, R. J. Faehl, M. V. Fazio, W. B. Haynes, and R. M. Stringfield, "Intense space-charge physics relevant to relativistic klystron amplifiers," *IEEE Trans. Plasma Sci.*, **22**, 719 (1994).
17. E. R. Colby, G. Caryotakis, W. R. Fowkes, and D. N. Smithe, "W-band sheet beam klystron simulations," High Energy Density Microwaves, AIP conference proceedings 474, American Institute of Physics, Woodbury, NY, 74 (1999).

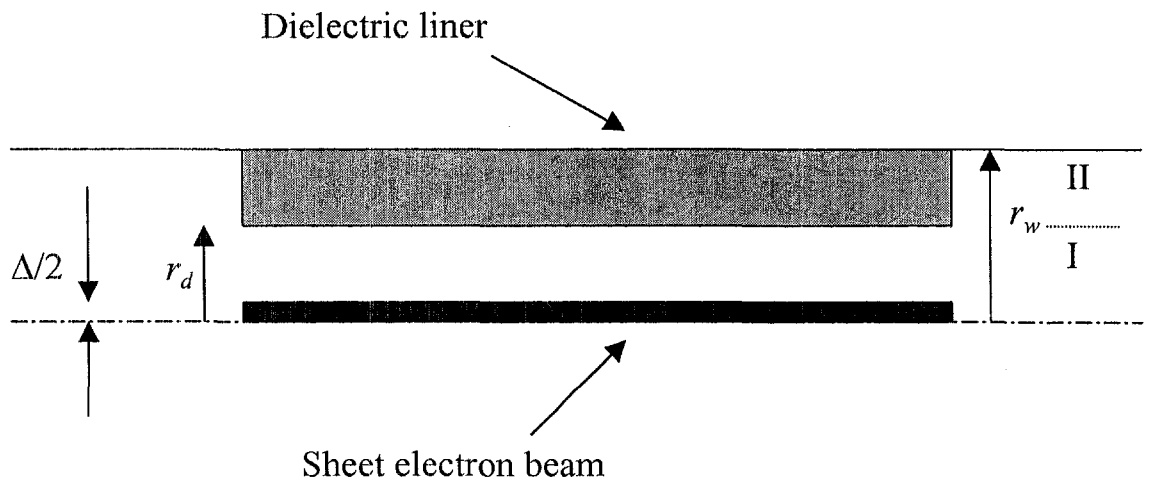


FIGURE 1. Notional planar dielectric Cherenkov maser geometry. The electron beam has total thickness of  $\Delta$ , the waveguide half height is  $r_w$ , and the dielectric liner has thickness  $r_w - r_d$ . The bottom dashed line is a symmetry plane.

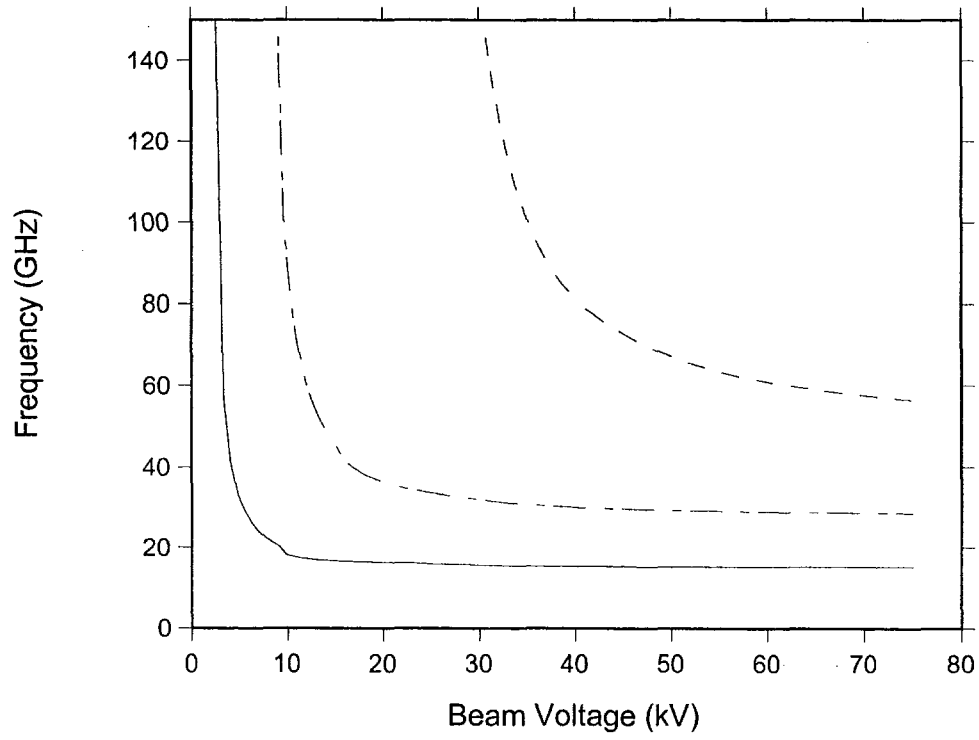


FIGURE 2. Frequency dependence on beam voltage and dielectric constant, for a 2 mm waveguide with  $\frac{1}{2}$  mm dielectric liner on top and bottom. The solid curve is for a relative dielectric constant of 10, the dot-dashed curve for a constant of 30, and the dashed curve for a constant of 100.



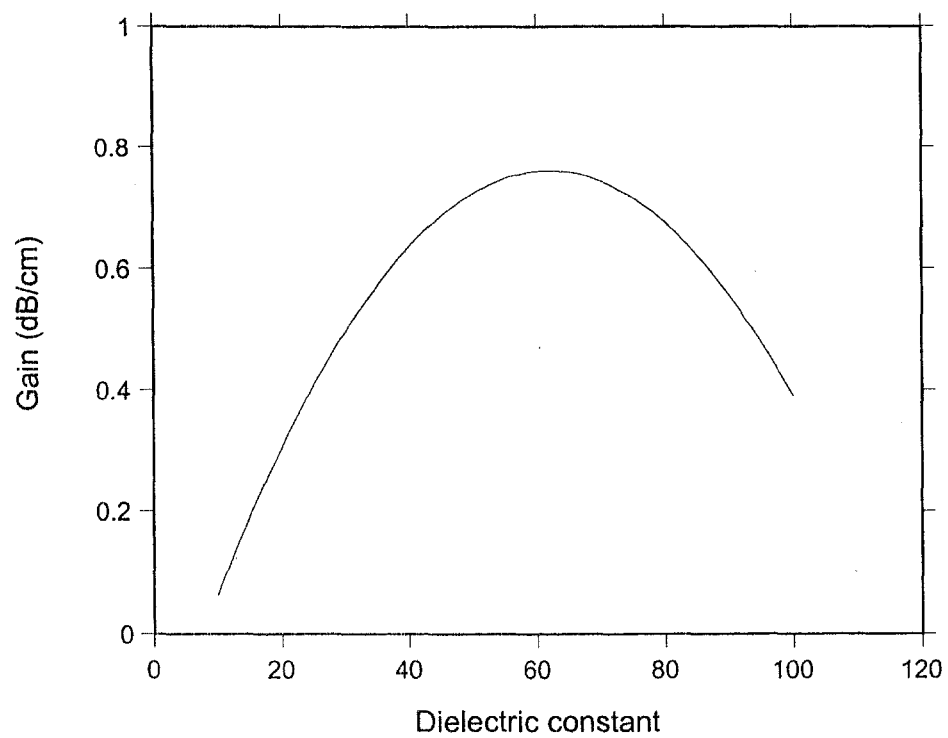


FIGURE 3. Gain versus dielectric constant, for a constant beam power of 75 kW.

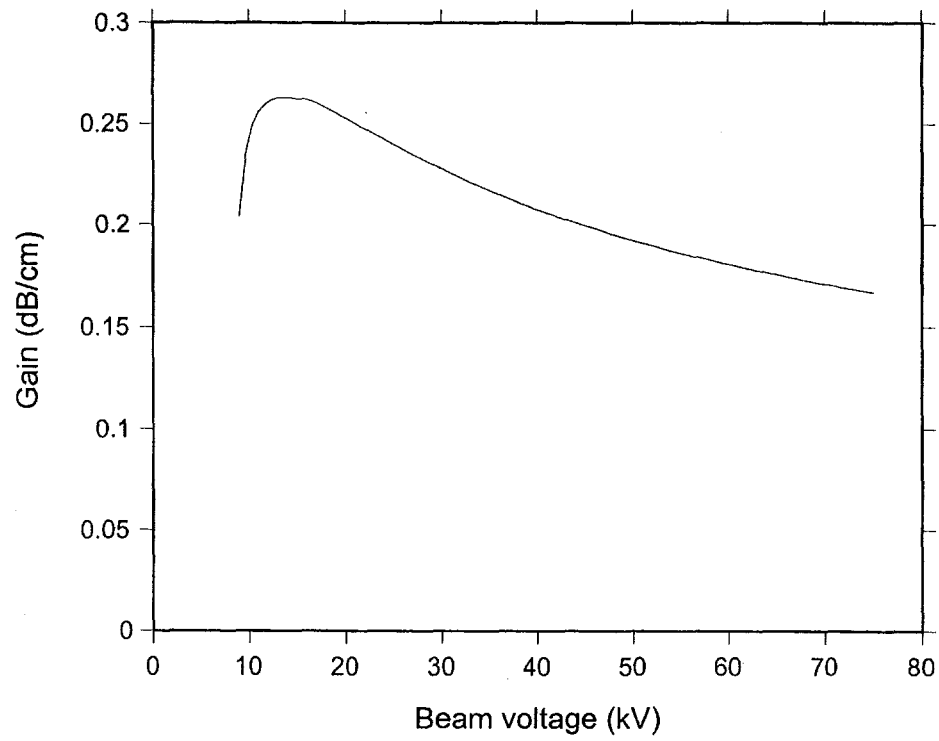


FIGURE 4. Gain versus beam voltage for a dielectric constant of 30 and for 1 A beam current.

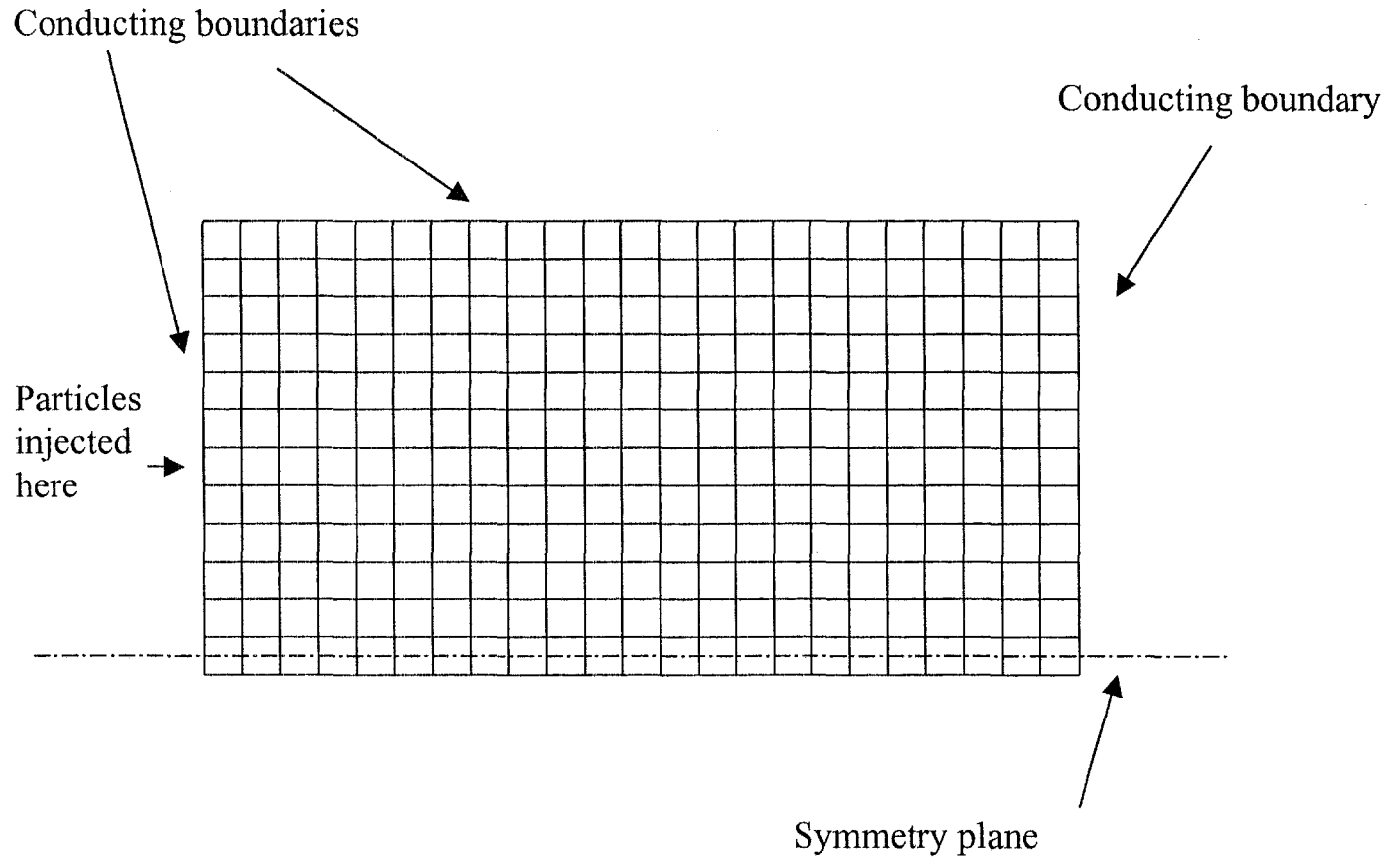


FIGURE 5. Simulation grid geometry. Index 1 runs from left to right, and index 2 runs from bottom to top, for a grid with 23 horizontal cells and 12 vertical cells. Grid cell (1,1) is in the lower left corner. The bottom row of cells is offset to establish the boundary conditions on the vertical electric field.

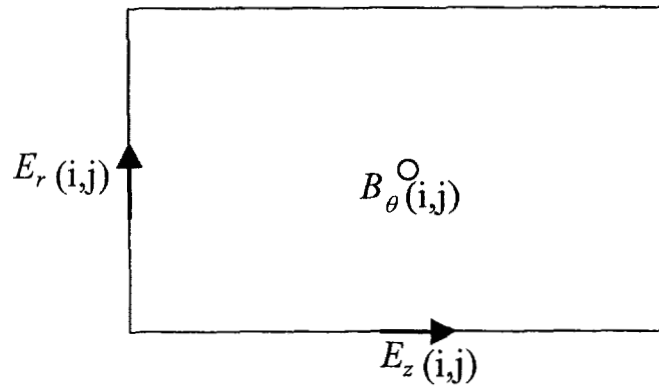


FIGURE 6. TM field components and locations for grid cell (i,j).

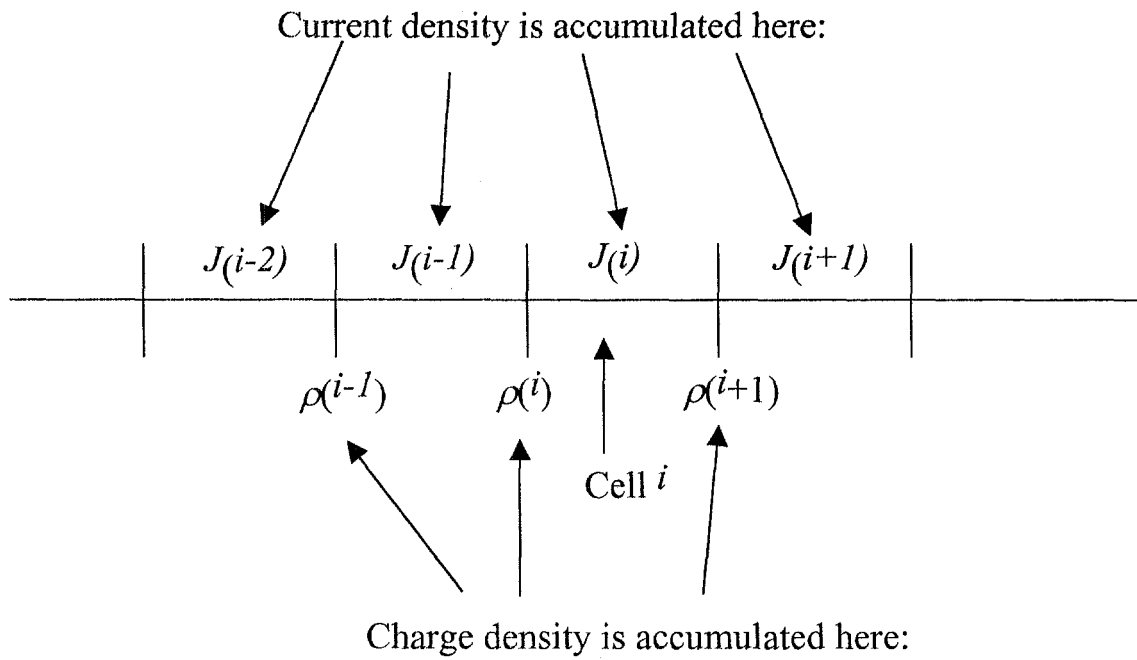
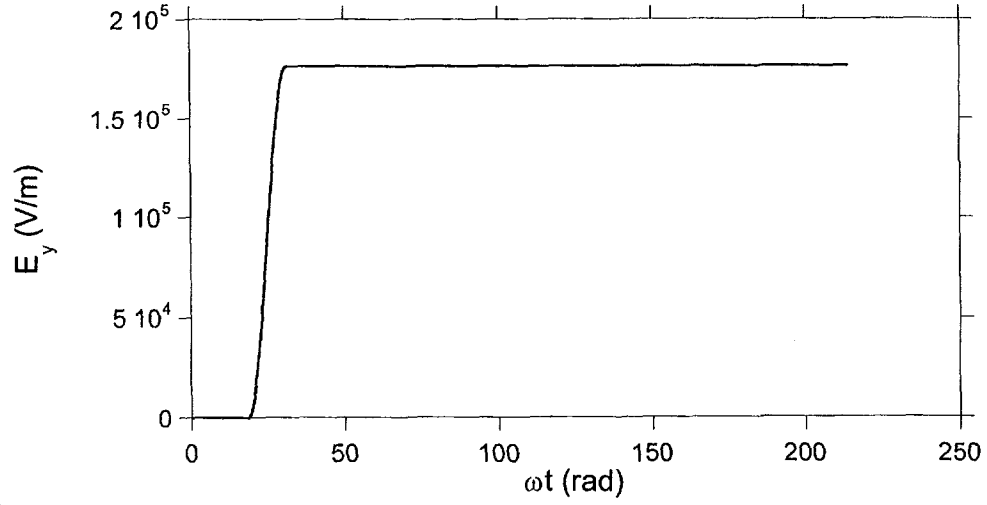
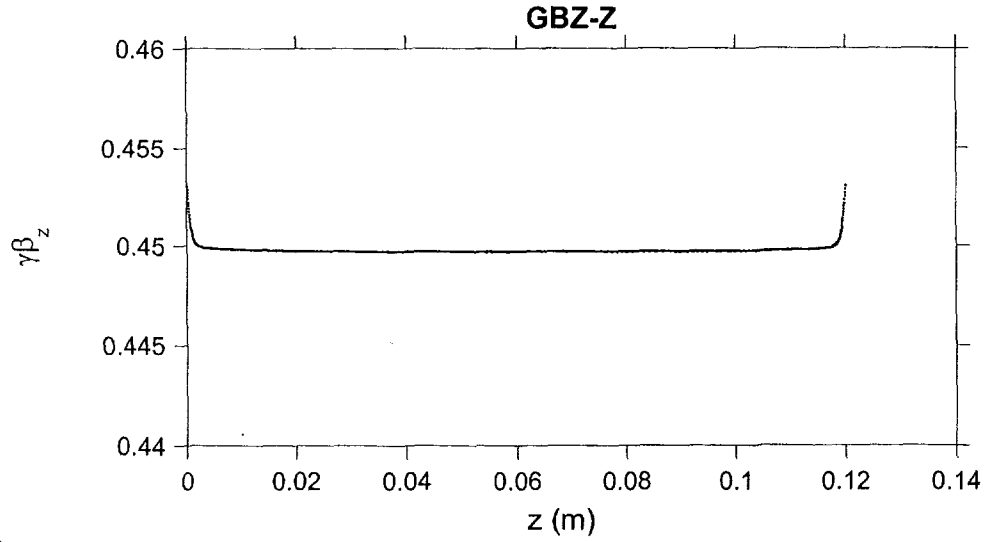


FIGURE 7. One-dimensional model for Morse and Nielson charge-conserving current algorithm. Charge density is assigned to mesh intersection points and current density is assigned to positions between the mesh intersection points.



(a)



(b)

FIGURE 8. (a) Vertical electric field above sheet beam as a function of time normalized to the radial frequency. (b) Axial momentum of the sheet beam within the simulation region showing potential depression of the particles.

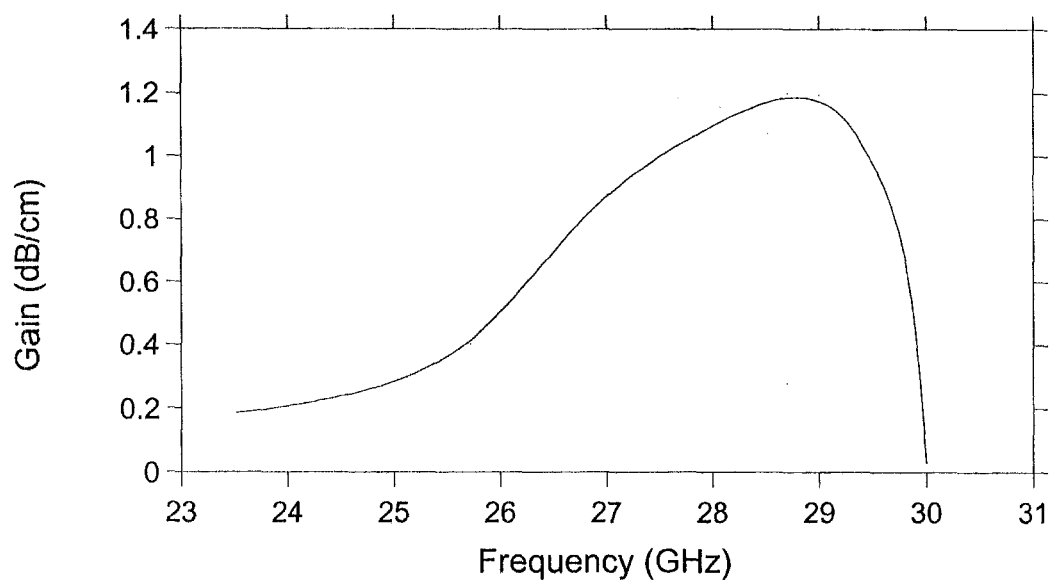


FIGURE 9. Gain versus frequency for the nominal sheet beam DCM case.

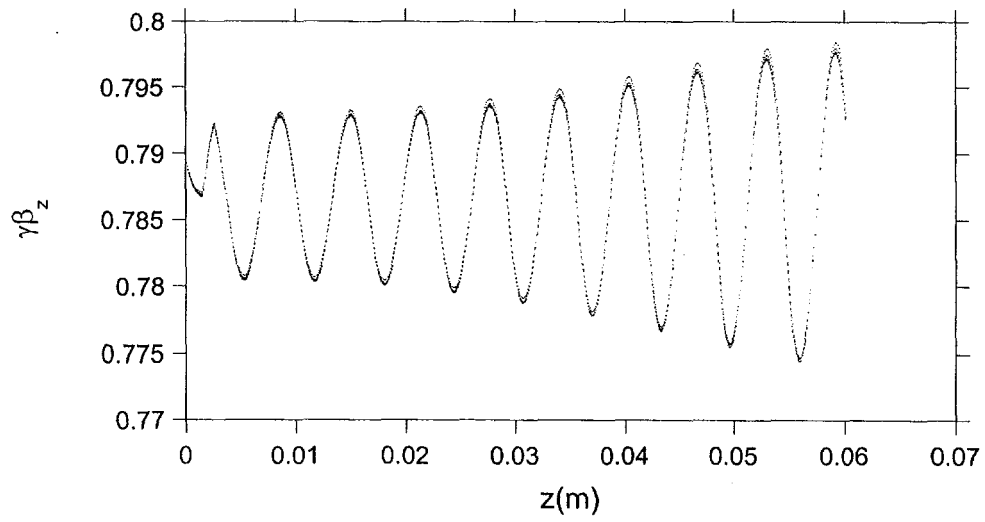


FIGURE 10. Axial momentum versus axial position in the simulation region. The exponential gain factor can be found by measuring the exponential growth in the velocity spread of the particles.



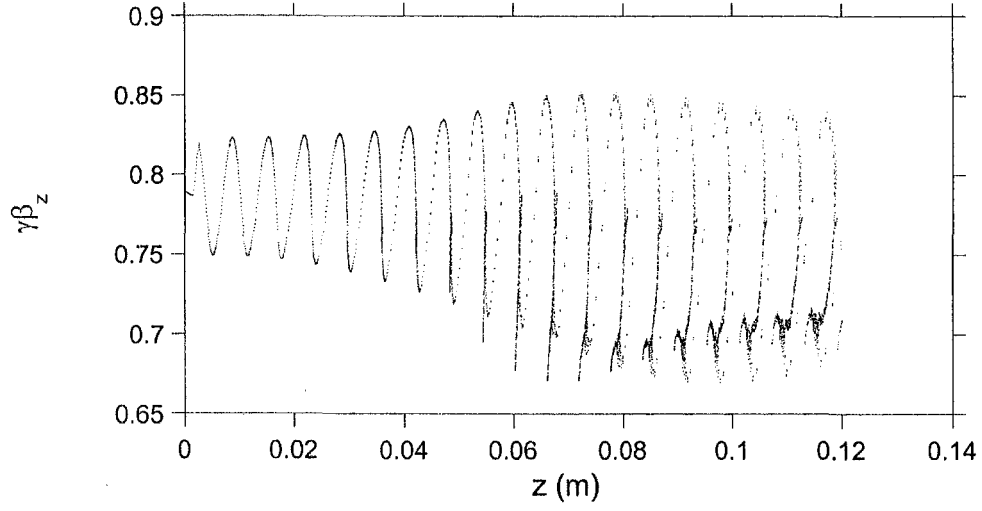


FIGURE 11. Axial momentum versus axial position in the simulation region, showing large signal saturation. This simulations corresponds to about 20% extraction efficiency.